PHYSICAL SCIENCES

On the remarkable resistance to oxidation by the Bi_{18}^- cluster

Jun Ma[1]†, Teng-Teng Chen[2,3,4]*†, Honglin Li[5]†, Dennis Bumüller[6], Florian Weigend[6], Tian Jian[4], Manfred M. Kappes[6,7], Detlef Schooss[6]*, Wan-Lu Li[5,8]*, Xiao-Peng Xing[1]*, Lai-Sheng Wang[4]*

The reactivity of Bi_n^- clusters (n = 2 to 30) with O_2 is found to display even-odd alternations. The open-shell even-sized Bi_n^- clusters are more reactive than the closed-shell odd-sized clusters, except Bi_{18}^-, which exhibits no observable reactivity toward O_2. We have investigated the structure and bonding of Bi_{18}^- to understand its remarkable resistance to oxidation. We find that the most stable structure of Bi_{18}^- consists of two Bi_8 cages linked by a Bi_2 dimer, where each atom is bonded to three neighboring atoms. Chemical bonding analyses reveal that each Bi uses its three 6p electrons to form three covalent bonds with its neighbors, resulting in a Bi_{18}^- cluster without any dangling bonds. We find that the robust Bi_{18} framework along with the totally delocalized unpaired electron is responsible for the surprising inertness of Bi_{18}^- toward O_2. The Bi_{18} framework is similar to that in Hittorf's phosphorus, suggesting the possibility to create bismuth nanoclusters with interesting structures and properties.

INTRODUCTION

Atomic clusters exhibit size-dependent chemical and physical properties. The high ratios of surface atoms and the presence of dangling bonds in general result in higher chemical reactivity for clusters than their bulk counterparts. However, certain clusters with special geometric and electronic structures can have enhanced chemical and thermodynamic stability, such as the fullerenes (1) or many metal clusters (2–5), which generally have high symmetries and large energy gaps between their highest occupied (HOMO) and lowest unoccupied (LUMO) molecular orbitals. Discovering clusters with enhanced chemical and thermodynamic stabilities remains one of the most important goals in cluster science ever since the discovery of the fullerenes (1).

Bismuth is the heaviest stable element and exhibits interesting electronic properties. Its low toxicity has earned it the reputation of being a "green metal" (6). Bismuth nanoparticles display quantum confinement effects, large magnetoresistance, and enhanced superconductivity (7–10). Supported bismuth nanoparticles can exhibit catalytic performance and enable ultralong-lifespan aqueous sodium storage (11). These interesting electronic properties have stimulated considerable interests in the syntheses of different bismuth nanostructures (12–15). For example, bismuth nanotubes have been synthesized (13, 14), and monolayer bismuthenes with unique electronic properties have been predicted (16, 17). Small bismuth clusters have also been studied (18–23). In particular, the electronic structures of size-selected Bi_n^- clusters were studied by photoelectron (PE) spectroscopy (PES) (20–22), and the Bi_5^- cluster was shown to be a planar aromatic system similar to $C_5H_5^-$ (21). The magnetic properties of gaseous Bi_n ($n \leq 13$) clusters were examined using the Stern-Gerlach experiment (23), and an even-odd oscillation was observed: Even-sized clusters are closed-shell and diamagnetic, whereas the odd-sized clusters carry a single unpaired electron and are paramagnetic. The structures of bismuth clusters have been studied computationally (24–29), suggesting low-lying structures containing small units of Bi_4, Bi_6, and Bi_8. Most of the bismuth atoms are found to be 3-coordinated, similar to the bonding pattern in bulk bismuth. The structures of Bi_n^+ (n = 4 to 14) have been probed by a combination of trapped ion electron diffraction (TIED) and ion mobility experiment (30), revealing that for $n > 8$, the clusters adopt prolate structures with coordination numbers of 3 and 4 and highly directional bonds. Despite the extensive studies on their electronic and atomic structures, the chemical reactivity of bismuth clusters has not been investigated and no chemically stable bismuth clusters have been discovered.

Here, we report a study of the chemical reactivity of Bi_n^- anionic clusters (n = 2 to 30) with O_2. We observe an even-odd oscillation, where the open-shell even-sized Bi_n^- clusters are found to be substantially more reactive than the closed-shell odd-sized clusters, except Bi_{18}^-, which shows no detectable reactivity with O_2. This remarkable resistance to oxidation is elucidated on the bases of the unique structure and bonding of the Bi_{18}^- cluster from both the PES and TIED experiments. We find that the Bi_{18}^- cluster consists of two Bi_8 cages linked by a Bi_2 dimer, which can be viewed as a molecular analog of the Hittorf's phosphorous (31) with remarkable chemical and thermodynamic stabilities and suggests that Hittorf-like low-dimensional bismuth nanostructures may be possible.

RESULTS

Chemical reactivity with O_2

The reactivity of Bi_n^- (n = 2 to 30) with O_2 is studied on an instrument composed of a magnetron sputtering cluster source, a continuous flow reactor and a time-of-flight (TOF) mass spectrometer (see Materials and Methods) (32, 33). Figure 1 shows the relative

[1]Shanghai Key Lab of Chemical Assessment and Sustainability and Department of Chemistry, Tongji University, 1239 Siping Road, Shanghai 200092, China. [2]Department of Chemistry, The Hong Kong University of Science and Technology, Clear Water Bay, Kowloon 999077, Hong Kong (SAR), China. [3]HKUST Shenzhen-Hong Kong Collaborative Innovation Research Institute, Futian, Shenzhen 518045, China. [4]Department of Chemistry, Brown University, Providence, RI 02912, USA. [5]Aiiso Yufeng Li Family Department of Chemical and Nano Engineering, University of California San Diego, La Jolla, CA 92093, USA. [6]Institute of Nanotechnology, Karlsruhe Institute of Technology (KIT), 76131 Karlsruhe, Germany. [7]Institute of Physical Chemistry, Karlsruhe Institute of Technology (KIT), 76131 Karlsruhe, Germany. [8]Program of Materials Science and Engineering, University of California San Diego, La Jolla, CA 92093, USA.

*Corresponding author. Email: tengtengchen@ust.hk (T.-T.C.); detlef.schooss@kit.edu (D.S.); wal019@ucsd.edu (W.-L.L.); xingxp@tongji.edu.cn (X.-P.X.); lai-sheng_wang@brown.edu (L.-S.W.).

†These authors contributed equally to this work.

reaction rates of Bi_n^- ($n = 2$ to 30) with O_2 by fitting the results obtained under different O_2 flows (i.e., concentrations). The relative reaction rates are normalized to that of Bi_{14}^-. We find that the very small Bi_n^- clusters ($n = 2$ to 4) reacted with O_2 extremely fast and no bare Bi_n^- clusters can be detected after exposure to O_2 even at low O_2 flows (fig. S1). Hence, we can only estimate a lower limit of their relative reaction rates (represented by the ↑ arrows in Fig. 1). For the very slow rates of some of the larger clusters, we can only estimate their higher limits (represented by the ↓ arrows in Fig. 1) due to the very weak signals of the reaction products. Figure 1 reveals a clear even-odd oscillation of the reaction rates for $n > 4$, where the even-sized Bi_n^- clusters are much more reactive than their odd-sized neighbors. The only exception is Bi_{18}^-, which has even lower reactivity than all other odd-sized clusters. The reactivity of Bi_{18}^- with O_2 is not measurable, as shown in the mass spectra in fig. S1. We do not observe any measurable oxidation products for Bi_{18}^- even when we increase the O_2 flow to 10 standard cubic centimeter per minute, the highest possible on our instrument. This inertness of Bi_{18}^- toward O_2 is remarkable, which must originate from its unique electronic and/or geometrical structure. To elucidate this extraordinary chemical stability of the Bi_{18}^- cluster, we have investigated its structure and electronic properties using PES and TIED together with theoretical calculations.

Global minimum structure searches

We performed global minimum searches for the structure of Bi_{18}^- using a "supervised" basin hopping algorithm implemented in our in-house San Diego Global Minimum Search (SDGMS) package (34), alongside a particle-swarm optimization (PSO) algorithm implemented in CALYPSO (35), both in conjunction with density functional theory (DFT) calculations. Further details can be found in Materials and Methods. The three lowest-energy structures are depicted in Fig. 2A, with their Cartesian coordinates provided in table S1. The lowest energy structure **I** (Fig. 2B) can be topologically described as comprising of two Bi_8 cages, connected by a Bi_2 dimer highlighted in blue.
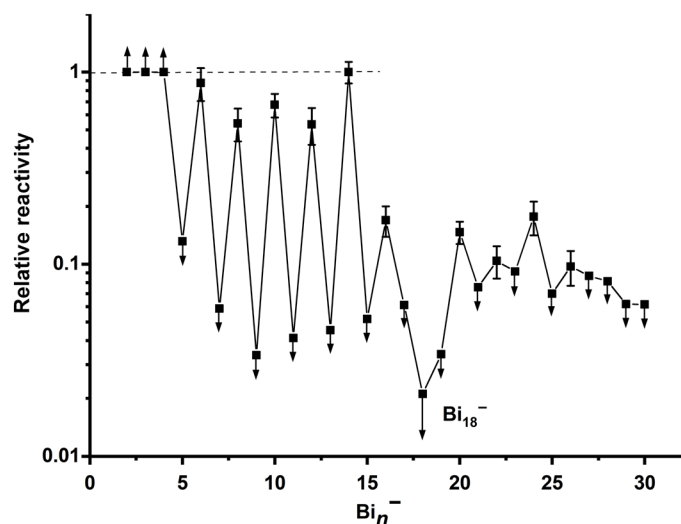
Each Bi_8 cage includes a square Bi_4 unit shaded in red, and a triangular pyramid Bi_4 cap. In structure **I** (C_s, $^2A'$), the relative orientation of the two Bi_8 units is inverted with respect to the connecting Bi_2 dimer. All the Bi—Bi bond lengths range from 3.02 to 3.21 Å (Fig. 2B), consistent with Pyykkö's single Bi—Bi bond distance (36). The other two low-lying isomers (**II** and **III**), both with C_{2v} symmetry, are structurally similar to the global minimum, except that in these isomers, the Bi_8 units are symmetric relative to the connecting Bi_2 dimer. Both are about 0.1 to 0.2 eV higher in energy than the global minimum, as calculated using the generalized gradient approximation (GGA) with the Perdew-Burke-Ernzerhof functional and triple-ζ basis set (PBE/TZP), as well as at the hybrid GGA PBE0/VTZ level. Thus, they are unlikely to have substantial populations under our experimental conditions. Structures **I**, **II**, and **III** can be regarded as stereoisomers, distinguished by different arrangements of the Bi_8 cages.

Photoelectron spectroscopy

The electronic structure of Bi_{18}^- is probed by PES using a magnetic-bottle TOF apparatus (see Materials and Methods) (37). Figure 3A shows the spectrum of Bi_{18}^- at 193 nm (6.424 eV), displaying well-resolved spectral features in the low binding energy side. The observed PES features are labeled with letters (X and A to H). The higher binding energy side is more congested: the labels I to L are only for the sake of discussion. A sharp ground-state peak (X) is observed, which is from detachment transition from the ground state of Bi_{18}^- to that of Bi_{18}, whereas peaks A to L all represent detachment transitions to excited electronic states of neutral Bi_{18}. The first vertical detachment energy (VDE) is measured from the maximum of peak X to be 2.50 eV and the first adiabatic detachment
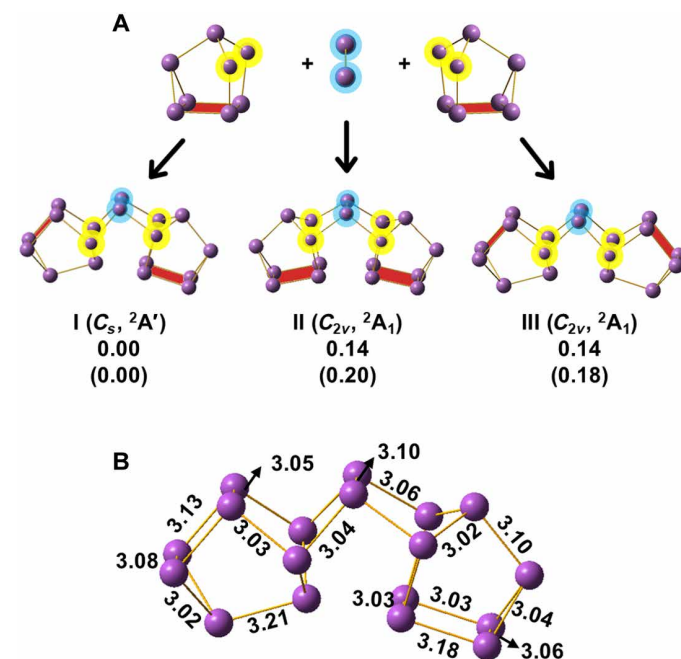

Fig. 1. Relative reactivity of Bi_n^- ($n = 2$–30) with O_2. All reaction rates are normalized to that of Bi_{14}^-. The ↑ arrows represent lower limits because the reactions are too fast. The ↓ arrows represent upper limits because the reactions are too slow. Note that the relative rate for Bi_{18}^- is negligible.

Fig. 2. The structures of Bi_{18}^-. (**A**) The global minimum **I** (C_s, $^2A'$) and two low-lying isomers **II** (C_{2v}, $^2A_1$) and **III** (C_{2v}, $^2A_1$), derived from two Bi_8 cages and a bridging Bi_2 dimer (blue). The two connecting Bi atoms on the Bi_8 cages are highlighted in yellow. Relative energies (in eV) are obtained from PBE/TZP and PBE0/VTZ (in parentheses). (**B**) Bond distances in Å of the global minimum **I**. The coordinates for the three structures are given in table S1.

energy (ADE) is measured from the onset of peak X to be 2.40 eV, which also represents the electron affinity of neutral Bi_{18}. The experimental VDEs of all the observed PES features are given in table S2. The sharp peak X indicates that there is little structural change between Bi_{18}^- and neutral Bi_{18}. The large energy gap (0.86 eV) between peaks X and A suggests that neutral Bi_{18} is closed-shell with a large HOMO-LUMO gap.

The simulated spectra of isomers **I** to **III**, obtained by using the ΔSCF-TDDFT (self-consistent field-time-dependent density functional theory) method (see Materials and Methods), are compared with the experimental spectrum in Fig. 3. The first VDEs and ADEs of all the three isomers are computed at PBE/TZP (table S3). The theoretical first VDEs of isomers **I** and **II** agree well with the experimental data, but that of isomer **III** shows a larger deviation. Among isomers **I** and **II**, the overall pattern of the simulated spectrum for isomer **I** agrees better with the experiment. In particular, the HOMO-LUMO gap of isomer **I** is in excellent agreement with the experimental observation, providing considerable credence for isomer **I** as the global minimum of Bi_{18}^-. We also optimized the neutral structure corresponding to isomer **I** and found that the neutral Bi_{18} structure is nearly identical to the anion, consistent with the sharp ground state peak observed in the PE spectrum.
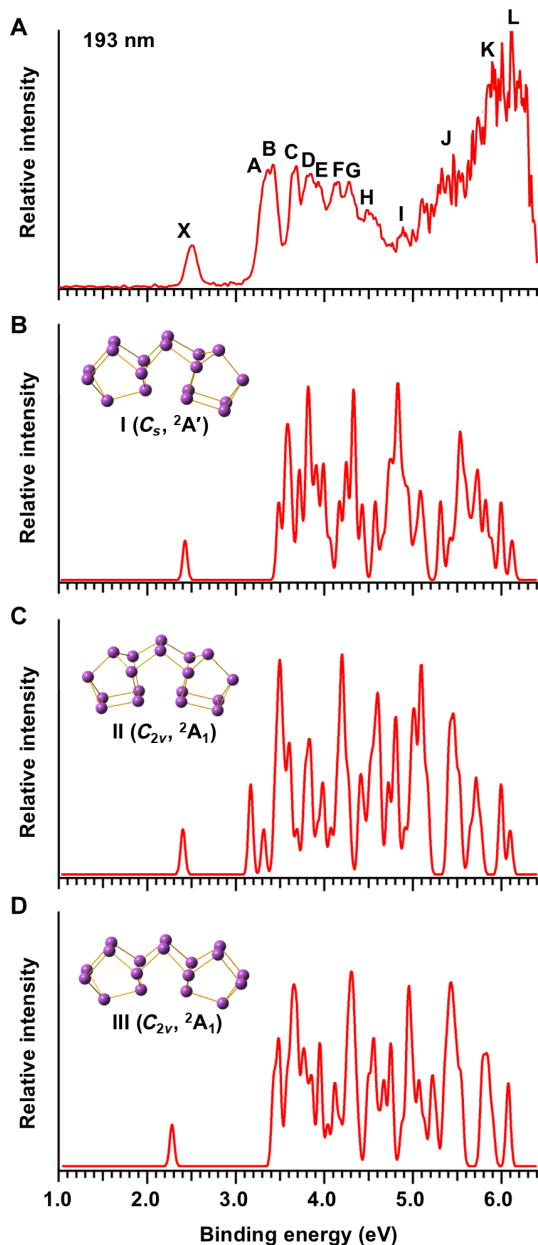
Trapped ion electron diffraction

The structure of Bi_{18}^- is further validated using the TIED technique (38, 39) (see Materials and Methods) by comparing the experimental scattering function to simulated scattering functions based on the three low-lying structures **I** to **III**, as shown in Fig. 4. The simulated scattering functions of structures **I** to **III** lead to profile factors of 6.1, 10.0, and 15.0%, respectively. The profile factor R_w is a quantitative measure of the agreement between the simulated and experimental molecular scattering functions. It is the lowest for structure **I** among the considered structures, thereby confirming that structure **I** is the experimentally probed structure and corroborating the global minimum structure obtained from the comparison between PES and the computed structures above.

Chemical bonding analysis of Bi_{18}^-

The bonding in the global minimum of Bi_{18}^- is analyzed using the adaptive natural density partitioning (AdNDP) approach (40), as shown in Fig. 5A. We found a $6s^2$ lone pair for each Bi atom. The
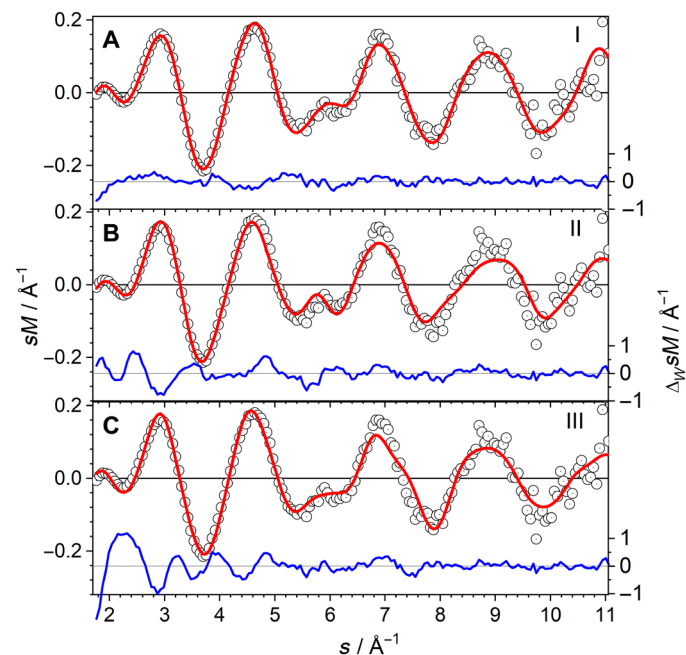

Fig. 3. Photoelectron spectroscopy. (**A**) The PE spectrum of Bi_{18}^- at 193 nm (6.424 eV). (**B** to **D**) The simulated spectra from the global minimum **I** and the two low-lying isomers (**II** and **III**) of Bi_{18}^-. The simulations were done at the TD-PBE/TZP level of theory (see Materials and Methods).

Fig. 4. Trapped ion electron diffraction. (**A** to **C**) Comparison of the experimental (circles) and simulated (red) molecular scattering functions for the global minimum **I** and the low-lying isomers **II** and **III** of Bi_{18}^-. The blue line in each panel shows the weighted residuals.

occupation number of the lone pairs (ON = 1.97 to 1.99 |e|) is close to the ideal value of 2.0 |e|, suggesting very little s-p hybridization similar to other Bi-containing clusters (41, 42). This is due to the relativistic effects that stabilize the 6s electron and destabilize the 6p electrons (43, 44). Each Bi atom uses its three 6p electrons to form three covalent bonds, yielding a total of 27 classical two-center two-electron (2c-2e) Bi—Bi σ bonds. In addition, we found an 18c-1e bond, which is completely delocalized over the Bi_{18} framework. The AdNDP analyses reveal a near perfect bonding situation in Bi_{18}^- without any dangling bond. The ideal bond angles should be 90° for bonding by the 6p orbitals. In fact, many bond angles in the Bi_{18}^- global minimum are around 90° (fig. S2A). The unpaired electron in Bi_{18}^- occupies the LUMO of neutral Bi_{18} [singly occupied molecular orbital (SOMO) in Fig. 5B]. Consistent with the AdNDP analyses, both the SOMO and the spin density (Fig. 5C) show that the unpaired electron is completely delocalized over the whole Bi_{18} framework.

Structures **I**, **II**, and **III** are stereoisomers and the only difference between them are the orientation of the two Bi_8 units relative to the Bi_2 bridge (Fig. 2A). The different orientation of the Bi_8 units results in slightly different bond angles at the Bi_2 bridge, 94° for **I**, 104° for **II**, and 89° for **III** (fig. S2). While the ideal bond angle for Bi without s-p hybridization is 90°, small participation of the 6s orbital in the bonding would lead to a bond angle somewhat above 90°. Thus, the 94° bond angle in structure **I** is probably optimal in this sense, underlying its slightly higher stability.

Understanding the inertness of Bi_{18}^- toward O_2
One-electron transfer was observed to be the key for the reactions of Ag_n^- and Au_n^- clusters with O_2, where a strong even-odd effect was observed (32, 45). The even-sized clusters with an unpaired electron and lower electron binding energies were readily reactive with O_2 to form $M_n(O_2^-)$ charge-transfer complexes (46–49), whereas the closed-shell odd-sized clusters with high electron binding energies are not reactive toward O_2. Except for the highly reactive small Bi_n^- (n = 2 to 4) clusters and Bi_{18}^-, a similar even-odd effect is observed for the reactivity of the Bi_n^- clusters with O_2 (Fig. 1). However, there are two notable differences between the O_2 reactivity of the Bi_n^- clusters and that of the coinage metal clusters. First, the odd-sized Bi_n^- clusters do exhibit reactivity, albeit much weaker than the even-sized clusters. Second, many Bi_n^- clusters can react with more than one O_2 molecule (fig. S1), suggesting that the reaction of the Bi_n^- clusters with O_2 is more complicated, not simply a one-electron transfer process. This is because Bi can form stable oxides, in contrast to Ag and Au, which are resistant to oxide formation.

The question is, why is the open-shell Bi_{18}^- cluster so inert toward O_2? The answer lies in the unique structure and bonding of this highly stable cluster. Even though the binding energy of the unpaired electron in Bi_{18}^- is relatively low, its totally delocalized nature (Fig. 5, B to D) is not favorable for one-electron transfer. Second, there is no dangling bond or unsaturated surface site on Bi_{18}^- for binding with O_2 or forming Bi—O bonds. Each Bi atom in Bi_{18}^- is covalently satisfied. Figure 6 shows the SOMO and spin density of Au_6^- and Au_{20}^-, two prototypical reactive gold clusters with O_2. Even though the unpaired electron in the gold clusters is also delocalized, there is more electron density in the apex sites (2, 50), which are coordinatively unsaturated and provide the reactive sites for O_2 (46–49). The TIED results on small Bi_n^+ clusters (n < 15) showed that all the global minima of these clusters contain 2- or
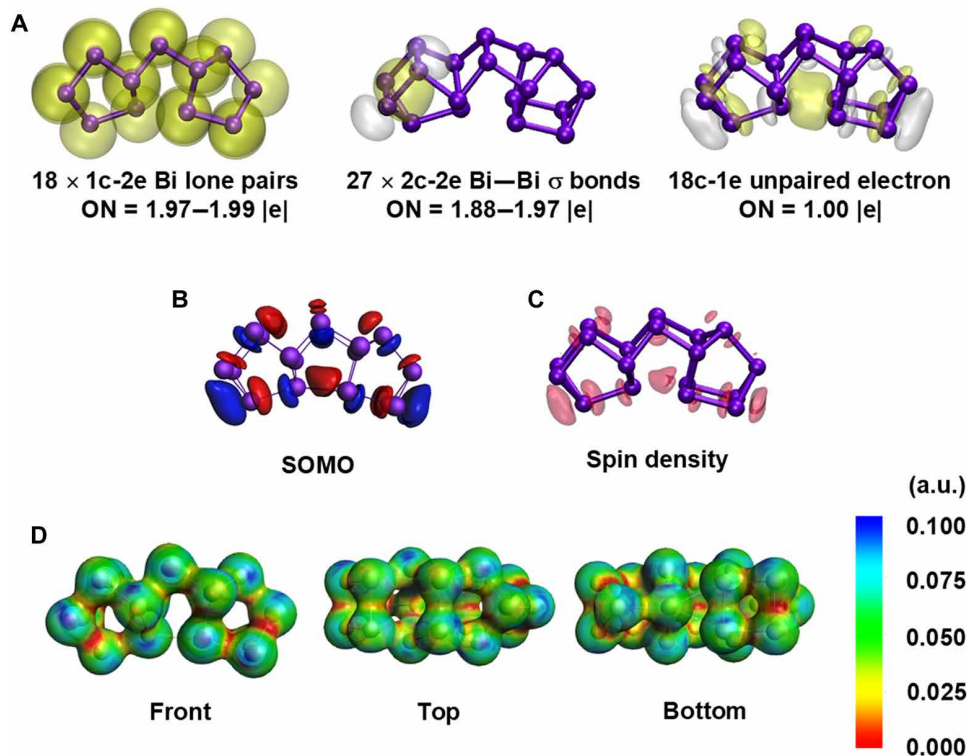

Fig. 5. Bonding analyses. (**A**) AdNDP bonding analyses for the global minimum structure **I** of Bi_{18}^-, showing 18 6s lone pairs and 27 Bi-Bi σ bonds, along with one delocalized 18c-1e bond. (**B**) The singly occupied molecular orbital (SOMO) of Bi_{18}^- (isovalue = 0.02 a.u.). (**C**) The spin density in the Bi_{18}^- cluster. (**D**) Electrostatic potential isovalue contour surfaces from different viewpoints (unit, a.u.).

4-coordination sites (*30*). It is expected that all the Bi_n^- clusters, other than Bi_{18}^-, should also contain undercoordinated Bi sites, which can be the active sites for O_2 reaction.

We performed calculations for O_2 binding on the global minimum structure **I** in various configurations, as shown in Fig. 7A. The results reveal that all adsorption energies are very small, demonstrating the weak binding ability of Bi_{18}^- with the O_2 molecule. Furthermore, we have conducted ab initio molecular dynamics (AIMD) simulations at room temperature on the strongest adsorption site (Fig. 7B). We find that the O_2 molecule is completely released from the Bi_{18}^- cluster after only 128 fs, indicating that this is not even a weak physical adsorption and demonstrating the unprecedented resistance to O_2 oxidation by Bi_{18}^-.
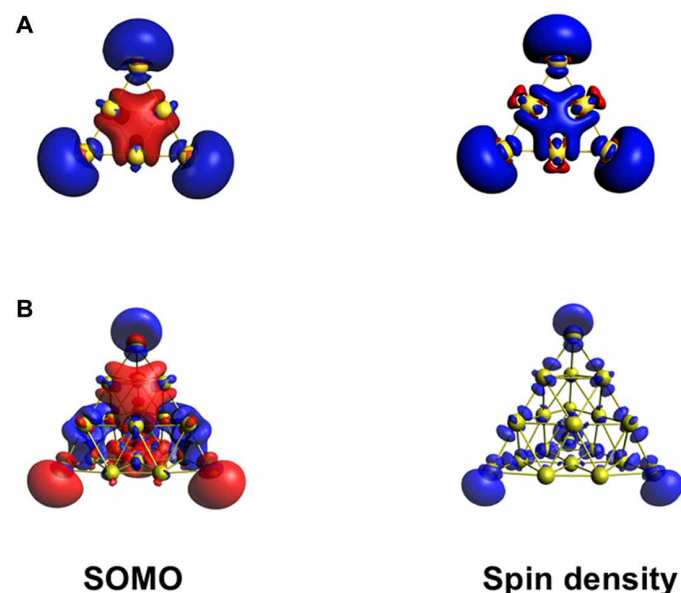

Fig. 6. Comparison of SOMO and spin density. The SOMO and spin density of (**A**) Au_6^- and (**B**) Au_{20}^-. The isovalue = 0.03 a.u.

The Bi_{18} cluster is a molecular bismuth analog of Hittorf's phosphorus

The neutral Bi_{18} cluster is a highly stable covalent molecular cluster with a large HOMO-LUMO gap (0.86 eV). Its structure is similar to that found in Hittorf's phosphorus (or violet phosphorus), consisting of similar P_8 units linked by P_2 units (*31*, *51*). Bulk bismuths or two-dimensional bithmuthenes adopt rhombohedral structures, which consist of puckered layered structures containing 3-coordinated atoms (*16*). All group V elements have such rhombohedral structures, but phosphorus has many more structural allotropes than its heavier congeners. In addition to the white, red, and black (rhombohedral) phosphorous, there also exists the Hittorf's phosphorous (*31*, *51*), which are polymeric forms P_8 or P_9 cages linked by P_2 or P_4 units. The Bi_8 unit in the Bi_{18} cluster is similar to the P_8 units in Hittorf's phosphorous. However, there are no similar bulk bismuth allotropes like the Hittorf's phosphorous. The present work shows that the Bi atoms in small clusters can exhibit strong covalent bonding, giving rise to stable molecular units analogous to its lighter congeners. The structure of Bi_{18} suggests that extended structures consisting of the Bi_8 motif linked by a Bi_2 unit may be possible, giving rise to Bi nanostructures analogous to Hittorf's phosphorous. On the basis of the remarkable resistance to oxidation by the Bi_{18}^- cluster, the putative Bi nanostructure should be highly stable both chemically and thermodynamically.

DISCUSSION

We report the discovery of a remarkably stable Bi_{18}^- cluster that is resistant to oxidation. Despite the presence of an unpaired electron, the unique structure and bonding characteristics of Bi_{18}^- result in its inertness toward O_2. The global minimum of the Bi_{18}^- cluster, along with its two next lowest-lying isomers, consists of two Bi_8 cages linked by a Bi_2 dimer with varying arrangements of the Bi_8 cages, similar to that in the Hittorf's phosphorus. Each Bi atom forms three covalent bonds, leading to a highly stable structure with no dangling bonds. Theoretical calculations confirmed the weak binding affinity of Bi_{18}^- for O_2 molecules, with complete desorption
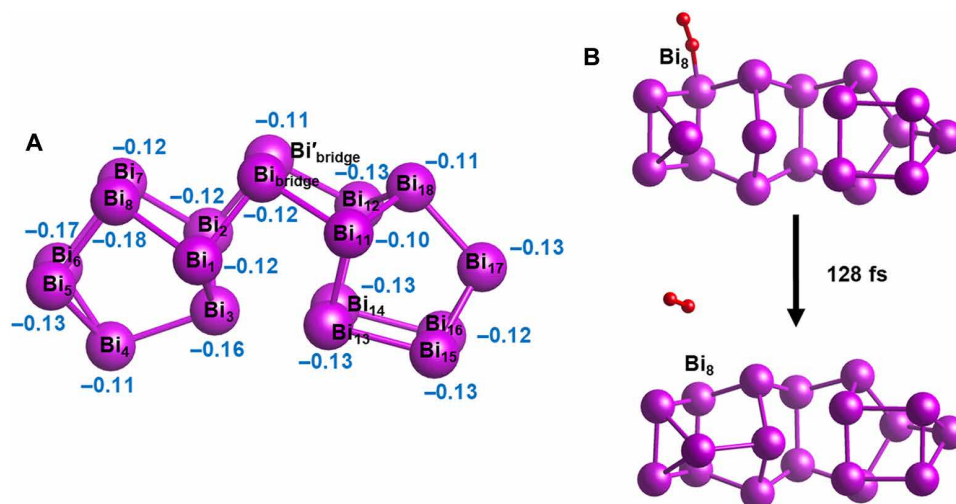

Fig. 7. Interaction of O_2 with B_{18}^-. (**A**) Adsorption energies (eV) of O_2 on different sites of B_{18}^- at the PBE-D3/TZV2P level. (**B**) AIMD simulation of the adsorbed O_2 undergoing desorption after 128 fs.

occurring at room temperature. The high chemical stability of the Bi_{18}^- cluster suggests the potential for creating Bi nanostructures analogous to Hittorf's phosphorus, which may exhibit interesting electronic properties. Recent research on bismuth-based metal clusters (52, 53) suggests promising prospects for synthesizing stable Bi_{18}-containing nanoclusters.

MATERIALS AND METHODS

Reactions of Bi_n^- with O_2

The reactivity of Bi_n^- ($n = 2$ to 30) with O_2 was studied on an instrument composed of a magnetron sputtering cluster source, a continuous flow reactor and a TOF mass spectrometer (32, 33). In brief, clusters were generated in the source chamber and entered the flow reactor together with the helium buffer gas. The nascent clusters were thermalized to the temperature of the reactor maintained at 120 K and then reacted with O_2, which was introduced downstream. After passing through a skimmer at the end of the flow reactor, the oxidized products and the unreacted clusters were analyzed by the TOF mass spectrometer. The intensities of individual Bi_n^- clusters with O_2 flow (I) and without O_2 (I_0) were measured at various O_2 flow rates. The relative reaction rates were obtained by linearly fitting $ln(I/I_0)$ versus the O_2 flow rate.

Photoelectron spectroscopy

The PE spectrum of Bi_{18}^- was obtained using a magnetic-bottle TOF PE spectrometer coupled with a laser vaporization supersonic cluster source, details of which have been described previously (37). In brief, bismuth clusters were produced by laser vaporization of a Bi disk target followed by supersonic expansion with a helium carrier gas seeded with 5% argon. Negatively charged clusters were analyzed by a TOF mass spectrometer perpendicular to the cluster beam. The Bi_{18}^- cluster of current interest was mass selected and decelerated before being photodetached by the 193-nm (6.424 eV) radiation from an ArF excimer laser. The resolution of the apparatus was around 2.5%, that is, about 25 meV for 1-eV electrons.

Trapped ion electron diffraction

The structure of Bi_{18}^- was determined experimentally by comparing scattering functions from the Karlsruhe TIED apparatus and simulated scattering functions based on candidate structures form DFT calculations. Details of the TIED experiment and the data analysis have been described elsewhere (38, 39) and only a brief description of the experimental procedure is given here. About 10^5 to 10^6 Bi_{18}^- clusters, generated from a magnetron sputtering source (54), were stored in a radio-frequency quadrupole ion trap and thermalized through collisions with a He buffer gas to a temperature of 95 ± 5 K. The ion cloud was irradiated by an electron beam (40 keV, ca. 2 to 3 μA) from a long focal length electron gun. Diffracted electrons from the clusters were detected by a phosphor screen assembly and integrated on an external charge-coupled device camera. A reference picture was accumulated by repeating the sequence without cluster ions in the trap. After typically accumulating several hundred such electron scattering exposures, the background-corrected diffraction pictures were radially averaged, yielding the total scattering I^{tot} as a function of the scattering angle θ represented by the electron momentum transfer $s = (4\pi/\lambda)\sin(\theta/2)$ as function of the electron wavelength λ. Considering the atomic scattering intensity I^{at} and an additional a priori unknown and unspecific flat background

I^{back}, the experimental reduced molecular scattering function is calculated as

$$sM^{expt} = s\left(I^{tot} - I^{at} - I^{back}\right) / I^{at}$$

The theoretical reduced molecular scattering function is approximated by

$$sM^{theo} = S_c \sum_{i}^{N} \sum_{j \neq i}^{N} \exp\left(-\frac{l_{ij}^2}{2}s^2\right) |f_i(s)||f_j(s)| \cos(\eta_i - \eta_j) \frac{\sin(sk_s r_{ij})}{k_s r_{ij}}$$

where N is the number of atoms in the cluster, S_c and k_s are scaling factors for the amplitudes and distances, f_i and η_i are partial wave elastic scattering amplitude and phase, and r_{ij} the distance between two atoms in the cluster. l_{ij}^2 are mean squared vibrational amplitudes (55) and account for thermal vibrations. Here, a single (averaged) value has been used.

The comparison of experimental data and the theoretical function was accomplished by a χ^2 fit minimizing the weighted differences by variation of S_c, k_s, l_{ij}, and parameters of the background polynomial I^{back}. Before the fit, sM^{theo} is convoluted by a Gaussian ($\sigma = 0.14$ Å^{-1}) to simulate experimental broadening effects, such as finite electron beam and cluster ion cloud size. Beam attenuation by scattering at the finite trap opening is taken into account by weighting sM^{theo} with an error function centered at the maximum theoretical scattering angle corresponding to $s = 14$ Å^{-1}. The level of agreement between experiment and model structure is then determined by a weighted profile factor (38), which is given by

$$R_w = \sqrt{\sum_i w_i \left(sM_i^{theo} - sM_i^{expt}\right)^2 / \sum_i w_i \left(sM_i^{expt}\right)^2}$$

The sums go over all experimental and corresponding theory data points. The weighting factors w_i are calculated from the error propagated SD of the experimental data.

Theoretical methods

A global minimum search was conducted to determine the most stable structures of the anion Bi_{18}^- and the neutral Bi_{18} using both a "supervised" Basin Hopping algorithm implemented in SDGMS (34) and the PSO algorithm in CALYPSO (35). DFT calculations were performed with SDGMS using the ADF 2024.1 program system (56). The generalized gradient approximation (GGA) PBE functional (57) was used with a Slater double-ζ basis set with one polarization function (DZP) (58). The frozen-core approximation was applied to the inner shells $[1s^2-4d^{10}]$ for bismuth in the all-electron ADF calculations. Relativistic effects were taken into consideration by the zeroth-order regular approximation (59). After obtaining the lowest lying isomers, larger triple-ζ basis sets (TZP) and hybrid PBE0 functional (60) were used to more accurately determine the relative energies. To eliminate prediction bias, we used a different prediction method PSO for neutral species, using the projector augmented wave method (61) as implemented in the periodic VASP code (62) in conjunction with CALYPSO.

PE spectra of the predicted global minimum structure and the other two C_{2v} stereoisomers were simulated using ΔSCF-TDDFT method (2) along with the PBE functional. The first VDE (VDE1) was computed as the energy difference between the anionic ground state and the corresponding neutral state at the anion's geometry. The ADE was calculated as the energy difference between the anionic

and neutral species at their respective optimized geometries. To simulate the PE spectra, each VDE was fitted with a Gaussian function of 0.06 eV width. The relative intensities in the simulated PE spectra were empirically determined, with a value of one for singlet states and two for triplet states.

Chemical bonding analyses were performed using molecular orbital theory at the PBE/TZP level and the AdNDP method (40), which involves diagonalizing the first-order reduced density matrix to optimally converge the electron density description. During the search for multicenter two-electron (nc-2e) bonds, the density matrix is iteratively depleted of density corresponding to the appropriate bonding elements, generating 1c-2e, 2c-2e, and nc-2e bonds. These calculations were carried out using the Gaussian 09 package (63). Fully relativistic energy-consistent pseudopotentials (ECP-60MDF) (64) and the cc-pVTZ (VTZ) (65) basis set were used for bismuth (Bi).

The reactivity of Bi_{18}^- with O_2 was examined by calculating the adsorption energy of O_2 on different sites of Bi_{18}^- using the PBE functional corrected by D3 van der Waals dispersion (66), combined with TZV2P MOLOPT basis sets optimized for multigrid integration (67), as implemented in the CP2K package (68). Norm-conserving pseudopotentials (69) were using to describe the interactions between the frozen cores and the valence shell electrons. The cutoff value was set to 450 rydbergs, and the number of grids was set to 5. The simulation box size was 30 Å × 30 Å × 30 Å. During geometry optimizations, the convergence criteria were set to 3×10^{-3} bohr for atomic displacements and 4.5×10^{-4} hartree/bohr for forces. The ab initio molecular dynamics simulations were performed in the canonical (NVT) ensemble at 300 K using the Nose-Hoover thermostat algorithm (70) with a time step of 1 fs.

Supplementary Materials
This PDF file includes:
Figs. S1 and S2
Tables S1 to S3

REFERENCES AND NOTES

1. H. W. Kroto, J. R. Heath, S. C. O'Brien, R. F. Curl, R. E. Smalley, C$_{60}$: Buckminsterfullerene. *Nature* **318**, 162–163 (1985).
2. J. Li, X. Li, H. J. Zhai, L. S. Wang, Au$_{20}$: A tetrahedral cluster. *Science* **299**, 864–867 (2003).
3. D. E. Bergeron, P. J. Roach, A. W. Castleman, N. O. Jones, S. N. Khanna, Al cluster superatoms as halogens in polyhalides and as alkaline earths in iodide salts. *Science* **307**, 231–235 (2005).
4. L. F. Cui, L. S. Wang, Stable icosahedral hollow cage clusters: Stannaspherene (Sn$_{12}$$^{2-}$) and plumbaspherene (Pb$_{12}$$^{2-}$). *Int. Rev. Phys. Chem.* **27**, 139–166 (2008).
5. Y. Jia, C.-Q. Xu, C. Cui, L. Geng, H. Zhang, Y.-Y. Zhang, S. Lin, J. Yao, Z. Luo, J. Li, Rh19−: A high-spin super-octahedron cluster. *Sci. Adv.* **9**, eadi0214 (2023).
6. R. Mohan, Grenn bismuth. *Nat. Chem.* **2**, 336 (2010).
7. B. Weitzel, H. Micklitz, Superconductivity in granular systems built from well-defined rhombohedral Bi-clusters: Evidence for Bi-surface superconductivity. *Phys. Rev. Lett.* **66**, 385–388 (1991).
8. Y. W. Wang, J. S. Kim, G. H. Kim, K. S. Kim, Quantum size effects in the volume plasmon excitation of bismuth nanoparticles investigated by electron energy loss spectroscopy. *Appl. Phys. Lett.* **88**, 143106 (2006).
9. F. Y. Yang, K. Liu, K. Hong, D. H. Reich, P. C. Searson, C. L. Chien, Large magnetoresistance of electrodeposited single-crystal bismuth thin films. *Science* **284**, 1335–1337 (1999).
10. J. Heremans, C. M. Thrush, Y. M. Lin, S. Cronin, Z. Zhang, M. S. Dresselhaus, J. F. Mansfield, Bismuth nanowire arrays: Synthesis and galvanomagnetic properties. *Phys. Rev. B* **61**, 2921–2930 (2000).
11. H. Zhu, F. Wang, L. Peng, T. Qin, F. Kang, C. Yang, Inlaying bismuth nanoparticles on graphene nanosheets by chemical bond for ultralong-lifespan aqueous sodium storage. *Angew. Chem. Int. Ed.* **62**, e202212439 (2023).
12. T. Som, A. Simo, R. Fenger, G. V. Troppenz, R. Bansen, N. Pfänder, F. Emmerling, J. Rappich, T. Boeck, K. Rademann, Bismuth hexagons: Facile mass synthesis, stability and applications. *ChemPhysChem* **13**, 2162–2169 (2012).
13. Y. Li, J. Wang, Z. Deng, Y. Wu, X. Sun, D. Yu, P. Yang, Bismuth nanotubes: A rational low-temperature synthetic route. *J. Am. Chem. Soc.* **123**, 9904–9905 (2001).
14. R. Boldt, M. Kaiser, D. Köhler, F. Krumeich, M. Ruck, High-yield synthesis and structure of double-walled bismuth-nanotubes. *Nano Lett.* **10**, 208–210 (2010).
15. F. Pan, B. Peerless, S. Dehnen, Bismuth-based metal clusters —From molecular aesthetics to contemporary materials science. *Acc. Chem. Res.* **56**, 1018–1030 (2023).
16. M. Pumera, Z. Sofer, 2D monoelemental arsenene, antimonene, and bismuthene: Beyond black phosphorus. *Adv. Mater.* **29**, 1605299 (2017).
17. R.-W. Zhang, C.-W. Zhang, W.-X. Ji, S.-S. Yan, Y.-G. Yao, First-principles prediction on bismuthylene monolayer as a promising quantum spin hall insulator. *Nanoscale* **9**, 8207–8212 (2017).
18. R. E. Walstedt, R. F. Bell, Ionization and fragmentation of Bi microclusters by electron impact. *Phys. Rev. A* **33**, 2830–2832 (1986).
19. M. E. Geusic, R. R. Freeman, M. A. Duncan, Neutral and ionic clusters of antimony and bismuth: A comparison of magic numbers. *J. Chem. Phys.* **89**, 223–229 (1988).
20. M. L. Polak, J. Ho, G. Gerber, W. C. Lineberger, Photoelectron spectroscopy of negatively charged bismuth clusters: Bi$_2$$^-$, Bi$_3$$^-$, and Bi$_4$$^-$. *J. Chem. Phys.* **95**, 3053–3063 (1991).
21. H. J. Zhai, L. S. Wang, A. E. Kuznetsov, A. I. Boldyrev, Probing the electronic structure and aromaticity of pentapnictogen cluster anions Pn$_5$$^-$ (Pn = P, As, Sb, and Bi) using photoelectron spectroscopy and ab initio calculations. *J. Phys. Chem. A* **106**, 5600–5606 (2002).
22. M. Gausa, R. Kaschner, G. Seifert, J. H. Faehrmann, H. O. Lutz, K. H. Meiwes-Broer, Photoelectron investigations and density functional calculations of anionic Sb$_n$$^-$ and Bi$_n$$^-$ clusters. *J. Chem. Phys.* **104**, 9719–9728 (1996).
23. S. Yin, X. Xu, R. Moro, W. A. de Heer, Measurement of magnetic moments of free Bi$_N$ Mn$_M$ clusters. *Phys. Rev. B* **72**, 174410 (2005).
24. L. Gao, P. Li, H. Lu, S. F. Li, Z. X. Guo, Size- and charge-dependent geometric and electronic structures of Bi$_n$ (Bi$_n$$^-$) clusters (n = 2–13) by first-principles simulations. *J. Chem. Phys.* **128**, 194304 (2008).
25. J. M. Jia, G. B. Chen, D. N. Shi, B. L. Wang, Structural and electronic properties of Bi$_n$ (n = 2-14) clusters from density-functional calculations. *Eur. Phys. J. D* **47**, 359–365 (2008).
26. H. K. Yuan, H. Chen, A. L. Kuang, Y. Miao, Z. H. Xiong, Density-functional study of small neutral and cationic bismuth clusters Bi$_n$ and Bi$_n$$^+$ (n = 2–24). *J. Chem. Phys.* **128**, 094305 (2008).
27. A. D. Zdetsis, Theoretical predictions of a new family of stable bismuth and other group 15 fullerenes. *J. Phys. Chem. C* **114**, 10775–10781 (2010).
28. A. J. Karttunen, M. Linnolahti, T. A. Pakkanen, Structural and electronic trends among group 15 polyhedral fullerenes. *Theor. Chem. Acc.* **129**, 413–422 (2011).
29. J. Akola, N. Atodiresei, J. Kalikka, J. Larrucea, R. O. Jones, Structure and dynamics in liquid bismuth and Bi$_n$ clusters: A density functional study. *J. Chem. Phys.* **141**, 194503 (2014).
30. R. Kelting, A. Baldes, U. Schwarz, T. Rapps, D. Schooss, P. Weis, C. Neiss, F. Weigend, M. M. Kappes, Structures of small bismuth cluster cations. *J. Chem. Phys.* **136**, 154309 (2012).
31. M. Ruck, D. Hoppe, B. Wahl, P. Simon, Y. Wang, G. Seifert, Fibrous red phosphorus. *Angew. Chem. Int. Ed.* **44**, 7616–7619 (2005).
32. J. Ma, X. Cao, X. Xing, X. Wang, J. H. Parks, Adsorption of O$_2$ on anionic silver clusters: Spins and electron binding energies dominate in the range up to nano sizes. *Phys. Chem. Chem. Phys.* **18**, 743–748 (2016).
33. J. Ma, X. Cao, H. Liu, B. Yin, X. Xing, The adsorption and activation of NO on silver clusters with sizes up to one nanometer: Interactions dominated by electron transfer from silver to NO. *Phys. Chem. Chem. Phys.* **18**, 12819–12827 (2016).
34. J. Burkhardt, T. T. Chen, W. J. Chen, D. F. Yuan, W. L. Li, L. S. Wang, Probing the structures and lanthanum-lanthanum bonding in La$_2$B$_n$$^-$ (n = 4–6) clusters. *Inorg. Chem.* **63**, 17215–17224 (2024).
35. Y. Wang, J. Lv, L. Zhu, Y. Ma, CALYPSO: A method for crystal structure prediction. *Comput. Phys. Commun.* **183**, 2063–2070 (2012).
36. P. Pyykkö, Additive covalent radii for single-, double-, and triple-bonded molecules and tetrahedrally bonded crystals: A summary. *J. Phys. Chem. A* **119**, 2326–2337 (2015).
37. L. S. Wang, Photoelectron spectroscopy of size-selected boron clusters: From planar structures to borophenes and borospherenes. *Int. Rev. Phys. Chem.* **35**, 69–142 (2016).
38. D. Schooss, M. N. Blom, J. H. Parks, B. von Issendorff, H. Haberland, M. M. Kappes, The structures of Ag$_{55}$$^+$ and Ag$_{55}$$^-$: Trapped ion electron diffraction and density functional theory. *Nano Lett.* **5**, 1972–1977 (2005).
39. D. Schooss, M. M. Kappes, Trapped ion electron diffraction of metal cluster ions, in *Encyclopedia of Interfacial Chemistry*, K. Wandelt, Ed. (Elsevier, 2018), pp. 567–579.
40. D. Y. Zubarev, A. I. Boldyrev, Developing paradigms of chemical bonding: Adaptive natural density partitioning. *Phys. Chem. Chem. Phys.* **10**, 5207–5217 (2008).
41. T. Jian, L. F. Cheung, T. T. Chen, L. S. Wang, Bismuth-boron multiple bonding in BiB$_2$O$^-$ and Bi$_2$B$^-$. *Angew. Chem. Int. Ed.* **56**, 9551–9555 (2017).

42. S. Pande, T. Jian, N. S. Khetrapal, L. S. Wang, X. C. Zeng, Structural evolution of gold-doped bismuth clusters $AuBi_n^-$ ($n = 4–8$). *J. Phys. Chem. C* **122**, 6947–6954 (2018).

43. P. Pyykko, Relativistic effects in structural chemistry. *Chem. Rev.* **88**, 563–594 (1988).

44. Y. L. Wang, H. S. Hu, W. L. Li, F. Wei, J. Li, Relativistic effects break periodicity in group 6 diatomic molecules. *J. Am. Chem. Soc.* **138**, 1126–1129 (2016).

45. B. E. Salisbury, W. T. Wallace, R. L. Whetten, Low-temperature activation of molecular oxygen by gold clusters: A stoichiometric process correlated to electron affinity. *Chem. Phys.* **262**, 131–141 (2000).

46. D. Stolcic, M. Fischer, G. Gantefor, Y. D. Kim, Q. Sun, P. Jena, Direct observation of key reaction intermediates on gold clusters. *J. Am. Chem. Soc.* **125**, 2848–2849 (2003).

47. R. Pal, L. M. Wang, Y. Pei, L. S. Wang, X. C. Zeng, Unraveling the mechanisms of O_2 activation by size-selected gold clusters: Transition from superoxo to peroxo chemisorption. *J. Am. Chem. Soc.* **134**, 9438–9445 (2012).

48. A. P. Woodham, G. Meijer, A. Fielicke, Activation of molecular oxygen by anionic gold clusters. *Angew. Chem. Int. Ed.* **51**, 4444–4447 (2012).

49. N. S. Khetrapal, D. Deibert, R. Pal, L. F. Cheung, L. S. Wang, X. C. Zeng, How O_2-binding affects structural evolution of medium even-sized gold clusters Au_n^- ($n = 20–34$). *J. Phys. Chem. Lett.* **12**, 3560–3570 (2021).

50. H. J. Zhai, B. Kiran, B. Dai, J. Li, L. S. Wang, Unique CO chemisorption properties of gold hexamer: $Au_6(CO)_n^-$ ($n = 0–3$). *J. Am. Chem. Soc.* **127**, 12098–12106 (2005).

51. G. Schusteritsch, M. Uhrin, C. J. Pickard, Single-layered Hittorf's phosphorus: A wide-bandgap high mobility 2D materials. *Nano Lett.* **16**, 2975–2980 (2016).

52. F. Pan, B. Peerless, S. Dehnen, Bismuth-based metal clusters—From molecular aethetics to contemporary materials science. *Acc. Chem. Res.* **56**, 1018–1030 (2023).

53. C. C. Shu, D. W. Szczepanik, A. Munoz-Castro, M. Sola, Z. M. Sun, $[K_2(Bi@Pd_{12}@Bi_{20})]^{4-}$: An endohedral inorganic fullerene with spherical aromaticity. *J. Am. Chem. Soc.* **146**, 14166–14173 (2024).

54. H. Haberland, M. Mall, M. Moseler, Y. Qiang, T. Reiners, Y. Thurner, Filling of micron-sized contact holes with copper by energetic cluster impact. *J. Vac. Sci. Technol. A* **12**, 2925–2930 (1994).

55. *CRC Handbook of Chemistry and Physics* (CRC Press, Boca Raton, FL, ed. 66, 1986), pp. B-203–219.

56. ADF, 2024.1, SCM, Theoretical Chemistry, Vrije Universiteit, Amsterdam, The Netherlands; http://www.scm.com.

57. J. P. Perdew, K. Burke, M. Ernzerhof, Generalized gradient approximation made simple. *Phys. Rev. Lett.* **77**, 3865–3868 (1996).

58. E. van Lenthe, E. J. Baerends, Optimized Slater-type basis sets for the elements 1–118. *J. Comput. Chem.* **24**, 1142–1156 (2003).

59. E. van Lenthe, E. J. Baerends, J. G. Snijders, Relativistic regular two-component Hamiltonians. *J. Chem. Phys.* **99**, 4597–4610 (1993).

60. C. Adamo, V. Barone, Toward reliable density functional methods without adjustable parameters: The PBE0 model. *J. Chem. Phys.* **110**, 6158–6170 (1999).

61. P. E. Blöchl, Projector augmented-wave method. *Phys. Rev. B* **50**, 17953–17979 (1994).

62. G. Kresse, J. Furthmüller, Efficiency of ab-initio total energy calculations for metals and semiconductors using a plane-wave basis set. *Comput. Mater. Sci.* **6**, 15–50 (1996).

63. M. J. Frisch, G. W. Trucks, H. B. Schlegel, G. E. Scuseria, M. A. Robb, J. R. Cheeseman, G. Scalmani, V. Barone, B. Mennucci, G. A. Petersson, H. Nakatsuji, M. Caricato, X. Li, H. P. Hratchian, A. F. Izmaylov, J. Bloino, G. Zheng, J. L. Sonnenberg, M. Hada, M. Ehara, K. Toyota, R. Fukuda, J. Hasegawa, M. Ishida, T. Nakajima, Y. Honda, O. Kitao, H. Nakai, T. Vreven, J. A. Montgomery Jr., J. E. Peralta, F. Ogliaro, M. Bearpark, J. J. Heyd, E. Brothers, K. N. Kudin, V. N. Staroverov, R. Kobayashi, J. Normand, K. Raghavachari, A. Rendell, J. C. Burant, S. S. Iyengar, J. Tomasi, M. Cossi, N. Rega, J. M. Millam, M. Klene, J. E. Knox, J. B. Cross, V. Bakken, C. Adamo, J. Jaramillo, R. Gomperts, R. E. Stratmann, O. Yazyev, A. J. Austin, R. Cammi, C. Pomelli, J. W. Ochterski, R. L. Martin, K. Morokuma, V. G. Zakrzewski, G. A. Voth, P. Salvador, J. J. Dannenberg, S. Dapprich, A. D. Daniels, Ö. Farkas, J. B. Foresman, J. V. Ortiz, J. Cioslowski, D. J. Fox, *Gaussian 09 Revision C.01* (Gaussian Inc., 2009).

64. B. Metz, H. Stoll, M. Dolg, Small-core multiconfiguration-Dirac–Hartree–Fock-adjusted pseudopotentials for post-d main group elements: Application to PbH and PbO. *J. Chem. Phys.* **113**, 2563–2569 (2000).

65. K. A. Peterson, D. Figgen, E. Goll, H. Stoll, M. Dolg, Systematically convergent basis sets with relativistic pseudopotentials. II. Small-core pseudopotentials and correlation consistent basis sets for the post-d group 16–18 elements. *J. Chem. Phys.* **119**, 11113–11123 (2003).

66. S. Grimme, J. Antony, S. Ehrlich, H. Krieg, A consistent and accurate *ab initio* parametrization of density functional dispersion correction (DFT-D) for the 94 elements H-Pu. *J. Chem. Phys.* **132**, 154104 (2010).

67. J. VandeVondele, J. Hutter, Gaussian basis sets for accurate calculations on molecular systems in gas and condensed phases. *J. Chem. Phys.* **127**, 114105 (2007).

68. J. Hutter, M. Iannuzzi, F. Schiffmann, J. VandeVondele, cp2k: Atomistic simulations of condensed matter systems. *Wiley Interdisc. Rev. Comput. Mol. Sci.* **4**, 15–25 (2014).

69. S. Goedecker, M. Teter, J. Hutter, Separable dual-space Gaussian pseudopotentials. *Phys. Rev. B* **54**, 1703–1710 (1996).

70. S. Nosé, A unified formulation of the constant temperature molecular dynamics methods. *J. Chem. Phys.* **81**, 511–519 (1984).